PCCP

PAPER

View Article Online
View Journal | View Issue

Check for updates

Cite this: *Phys. Chem. Chem. Phys.*, 2023, **25**, 15391

# Development of high refractive index UiO-66 framework derivatives *via* ligand halogenation†‡

Marvin Treger, [ab] Adrian Hannebauer, [a] Peter Behrens [ab] and Andreas M. Schneider *[ab]

Received 22nd March 2023,
Accepted 16th May 2023

DOI: 10.1039/d3cp01291c

rsc.li/pccp

UiO-66 is a Zr-based metal–organic framework (MOF) with exceptional chemical and thermal stability. The modular design of a MOF allows the tuning of its electronic and optical properties to obtain tailored materials for optical applications. Making use of the halogenation of the 1,4-benzenedicarboxylate (*bdc*) linker, the well-known monohalogenated UiO-66 derivatives were examined. In addition, a novel diiodo *bdc* based UiO-66 analogue is introduced. The novel UiO-66-$I_2$ MOF is fully characterized experimentally. By applying density functional theory (DFT), fully relaxed periodic structures of the halogenated UiO-66 derivatives are generated. Subsequently, the HSE06 hybrid DFT functional is used to calculate the electronic structures and optical properties. The obtained band gap energies are validated with UV-Vis measurements to assure a precise description of the optical properties. Finally, the calculated refractive index dispersion curves are evaluated underlining the capabilities to tailor the optical properties of MOFs by linker functionalization.

Open Access Article. Published on 19 May 2023. Downloaded on 12/5/2025 2:59:33 AM.
This article is licensed under a Creative Commons Attribution 3.0 Unported Licence.

## Introduction

Metal–organic frameworks (MOFs) are a prominent class of porous organic–inorganic hybrid materials built up by inorganic building units (IBUs) connected by organic ligands acting as linkers.[1,2] Due to the intrinsic porosity of the frameworks, MOFs have a large potential with regard to classical applications of porous materials, like catalysis, gas separation, gas storage, or gas sensing.[3–5]

Apart from these traditional applications for porous materials, the use of MOFs as materials for optical applications has risen in the last years.[6–9] Compared to classical materials used in optics like polymers, glasses and metal oxides, the electronic and optical properties of MOFs can be tailored in a very broad range. This is due to their modular design paired with porosity allowing the deployment of different metal centers, linkers and guest molecules.[10–13] Additionally, optical properties of MOFs can be altered dynamically for example by reversible adsorption of guest molecules.[14,15] The unique modulation of the characteristics of a MOF by its design paired with the dynamically adjustable optical properties allows the development of new, highly adapted materials for optical applications as well as the design of novel optical systems. Moreover, the design and development of an optical system itself is not only driven by the available materials and their properties but also by their processability. Here MOFs offer the advantage of low temperature preparation routes facilitating simpler and cheaper production processes of optical systems, *e.g. via* layer-by-layer synthesis, direct crystallization or spin-coating techniques.[12,15,16]

One of the most promising family of MOFs is formed by Zr-based frameworks. Most of these compounds feature exceptional chemical and thermal stability due to their high metal–ligand bond strength, facilitating the development of Zr-based MOFs for practical applications.[17] Here, we focus on the prominent Zr-based MOF UiO-66 and its halogenated derivatives. The UiO-66 framework is built up from well-known $Zr_6$-containing IBUs formed by zirconium-oxo-hydroxo clusters ($Zr_6O_4(OH)_4$) which are 12-fold coordinated by 1,4-benzenedicarboxylate (*bdc*) linkers leading to an expanded cubic closed-packed structure.[18] The use of monohalogenated *bdc* linkers results in the halogenated UiO-66 derivatives denoted as UiO-66-F, UiO-66-Cl, UiO-66-Br and UiO-66-I sharing the UiO-66 topology and exhibiting a high chemical and thermal stability as well.[19–22] These halogenated derivatives are isostructural to UiO-66, but show differences in the porosity and chemical nature of the pores, as well as different electronic and optical properties.[23–25]

While optical properties of MOFs in terms of the absorption and emission of light and nonlinear effects have been focused in several studies, the refractive index (RI) as a basic optical property has only recently gathered increasing attention.[6,12,15]

[a] *Institute of Inorganic Chemistry, Leibniz University Hannover, Hannover, 30167, Germany. E-mail: andreas.schneider@acb.uni-hannover.de*
[b] *Cluster of Excellence PhoenixD (Photonics, Optics, and Engineering – Innovation Across Disciplines), Hannover, Germany*

† Dedicated to the memory of Professor Peter Behrens.

‡ Electronic supplementary information (ESI) available: Synthesis procedures, argon sorption isotherm, TG analysis, NMR analysis, UV-Vis spectra, details of DFT calculations. See DOI: https://doi.org/10.1039/d3cp01291c

Open Access Article. Published on 19 May 2023. Downloaded on 12/5/2025 2:59:33 AM.
This article is licensed under a Creative Commons Attribution 3.0 Unported Licence.

In addition, studies aiming on the evaluation and modulation of the RI of MOFs are rare, but changes of the RI due to external stimuli have been used as sensor signal in many applications.[26] However, knowledge of the RI is of importance for optical elements and systems like filters, mirrors, antireflective coatings, and wave guides, and some of these applications require high or low RI values or a combination of both.[27–30]

In a previous study, we explored the options of modulating the RI of UiO-66 type MOFs by linker functionalization to obtain materials with distinct optical properties having with the same topology and without changing the synthesis protocol.[31] These materials feature novel *bdc* linker-based push-pull motifs and were suited for near IR applications due to the absorption of light in the visible range. Here, we focus not only on the modulation of the RI, but also on the design of materials with a broad range of transparency, especially in the visible range to widen up the field of possible applications. Hence, we employ established halogenated versions of the terephthalate linker containing a single halogen atom and a novel dihalogenated linker depicted in Fig. 1. Aiming for high RI values, we do not examine the established dihalogenated UiO-66 derivatives but present a novel *bdc*-$I_2$-based UiO-66 derivative.[32] The introduction of halogen atoms into the *bdc* linker increases the polarizability and allows to modulate the band gap of the resulting MOF leading to tailored optical properties. To understand these effects on the electronic structure and optical properties, we characterize the halogenated UiO-66 derivatives by applying density functional theory (DFT). In a first step different exchange–correlation functionals and dispersion corrections within the (*meta*) generalised gradient approximation (GGA, *m*GGA) are assessed to obtain adequate structural descriptions of the UiO-66 analogues. Subsequently, we use the range-separated hybrid functional HSE06 to determine both, the electronic structure and optical properties of the fully relaxed UiO-66 structure and its halogenated derivatives with high accuracy.[33–36] By using carefully converged plane-wave basis sets and fully relaxed models we follow our previously published strategy to ensure a precise characterization.[31]

In addition to the computational studies, we report the synthesis of a novel dihalogenated UiO-66 derivative featuring a linker with two iodine atoms (2,5-diiodo-1,4-dicarboxylate) extending the series of experimentally accessible dihalogenated UiO-66 derivatives.[32] We fully characterized this novel MOF which is only the second framework containing this terephthalate linker with two iodine atoms in *para* position.[37] Furthermore, we determined the band gaps of all materials *via* UV-Vis diffuse reflectance spectroscopy (UV-Vis DRS) and compared them with the theoretical values.

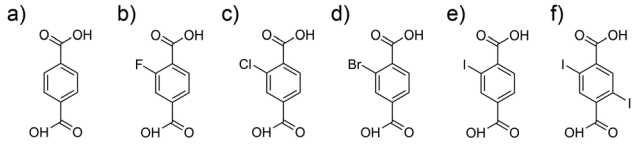


Fig. 1 UiO-66 linker molecules with (a) no functionalization, (b) fluoro, (c) chloro, (d) bromo, (e) iodo and (f) novel diiodo functionalization.

# Materials and methods

## Experimental details

UiO-66 was synthesized according to the synthetic route of Shearer *et al.*[38] All five UiO-66 derivatives reported were synthesized each in a 100 mL Pyrex glass vessel by dissolving specific amounts of $ZrCl_4$, water, formic acid and linker successively in DMF. The detailed synthesis procedure and amounts are given in ESI,‡ Section 1. The glass vessels were sealed and heated at 120 °C for 24 h. After cooling to room temperature, the precipitate was separated *via* centrifugation, washed once with DMF and twice with acetone and dried under vacuum overnight. For purification, the obtained powder materials were Soxhlet-extracted with acetone for 24 h and activated at 120 °C under vacuum.

Powder X-Ray diffraction (PXRD) was carried out in transmission mode using a Stoe Stadi-P diffractometer operated with Ge(111)-monochromatized CuK$\alpha_1$ radiation ($\lambda$ = 1.54060 Å). A Mythen 1 K detector was used and the diffractograms were recorded from 5 to 50° 2$\theta$. UV-Vis DRS was performed on MOF powders using a Praying Mantis device on a Cary 4000 from Agilent Technologies. For this purpose, the MOF powder was mortared with $BaSO_4$ to gain better quality measurements. For further characterization, digested MOF samples were analyzed *via* liquid $^1$H-NMR spectroscopy. Therefore, two different digestion methods were necessary depending on the functionalization of the linker. For UiO-66-F and UiO-66-Cl, 15 mg of MOF were dispersed in 800 μL of DMSO-D6, 15 μL of HF (40%) were added and the mixture was stirred overnight. After complete dissolution of the MOFs, small amounts of calcium chloride dihydrate were added to react with excess HF. Afterwards the suspension was decanted. All other MOF samples were digested according to the procedure of Chu *et al.*[39] For this purpose, 15 mg of MOF were digested in 1 M $(NH_4)_2CO_3$ solution in $D_2O$ for 2 h. $^1$H NMR spectra were recorded on a Bruker Ascend 400 MHz Spectrometer. Argon physisorption measurements were performed at 87 K on a Micromeritics 3Flex instrument. The samples (25 mg) were activated at 120 °C under secondary vacuum for 20 h. For the analysis of the data the associated software was used. BET areas were determined by the BET-auto function of the software and total pore volumes were calculated with single-point method at a relative pressure of 0.90. Scanning electron microscope (SEM) images were recorded with a JEOL JSM-6700F microscope using an accelerating voltage of 2 kV with a working distance of 3 mm. SEM samples were prepared by dispersion of small amounts of MOF powder in ethanol using an ultrasonic bath. The dispersion was dropped onto a polished graphite block and dried at room temperature. Thermogravimetric measurements were performed on a Netzsch STA 449 F5 Jupiter in synthetic air ($N_2$, $O_2$) with a heating rate of 5 K min$^{-1}$ using 10 mg of MOF powder.

## Computational details

All Kohn–Sham density functional theory calculations in this study were executed with the CASTEP code (version 20.1) which uses a plane-wave basis set and pseudopotentials.[40,41] The

 This journal is © the Owner Societies 2023

Open Access Article. Published on 19 May 2023. Downloaded on 12/5/2025 2:59:33 AM. This article is licensed under a Creative Commons Attribution 3.0 Unported Licence.

unmodified UiO-66 and its halogenated derivatives were modelled with primitive cells of the fcc lattice containing 114 atoms. The convergence of the plane-wave kinetic energy cutoff and the Brillouin zone sampling were determined by the change in lattice parameters of the primitive cells (see ESI,‡ Section 2) and set to 1000 eV for UiO-66 and 700 eV for the derivatives with $\Gamma$-point sampling. The pseudopotentials were generated on-the-fly with the Koelling–Harmon method to incorporate relativistic effects into the generated pseudopotentials.[42] To obtain the adequate basis set size and Brillouin zone sampling, all cells were fully relaxed employing the PBEsol exchange–correlation functional and "on-the-fly" generated ultra-soft pseudopotentials with an SCF convergence criterion of $5.0 \times 10^{-7}$ eV per atom.[43] The implemented low-memory Broyden–Fletcher–Goldfarb–Shanno (LBGFS) algorithm was used to generate structures with an energy change of less than $5.0 \times 10^{-6}$ eV per atom and a maximal force of 0.01 eV Å$^{-1}$ with the convergence threshold of the stress and maximal atom displacement set to 0.02 GPa and $5.0 \times 10^{-4}$ Å, respectively.

The basis set parameters obtained in the first step were used to assess different exchange–correlation (XC) functionals with regard to the lattice parameters of UiO-66 and its halogenated analogues in comparison with the experimental ones to generate precise structural models for further characterisation. Relying on the XC functional benchmark of our previous study, full cell relaxations were performed using the PBE expansion for solids (PBEsol) as well as its dispersion corrected form (PBEsol-TS) and the rSCAN *meta*-GGA functional.[31,44,45]

Subsequently, the best models of each benchmark were used to perform single point HSE06 hybrid DFT calculations to obtain accurate band structures, density of states (DOS) and the dispersion of the RI. All hybrid DFT calculations were carried out using $\Gamma$-point Brillouin zone sampling with the plane-wave kinetic energy cutoff values determined in the initial step of our simulation approach and a SCF convergence criterion of $10^{-9}$ eV per atom. In a final step, the optical properties were assessed by applying the tools provided with the CASTEP code to evaluate the electronic structure, calculate the complex dielectric function and subsequently the dispersion of the index of refraction.[46]

## Results and discussion

This study deals with the electronic and optical properties of halogenated UiO-66-type MOFs containing the linker molecules shown in Fig. 1. Of these, UiO-66 as well as its monohalogenated derivatives are well-known. Additionally, we have synthesized a novel compound, UiO-66-$I_2$ which is built by the terephthalate linker with two iodine atoms in *para* position. At first, we discuss the characterization of the synthesized MOFs. Afterwards, we focus on the results of the calculated electronic and optical properties of the MOFs in a second part.

### Experimental studies on halogenated UiO-66-type MOFs

The synthesis of the UiO-66 derivatives was carried out using the modulation approach with formic acid in DMF, which was introduced for the Zr-MOFs by our group.[47] By using this approach, the well-known halogenated UiO-66 derivatives, as well as the novel UiO-66-$I_2$, were obtained with a high crystallinity as proven by the PXRD measurements depicted in Fig. 2. UV-Vis DRS measurements show that UiO-66 and its derivatives only exhibit absorption in the UV region. UiO-66 shows a single absorption maximum with a small shoulder at higher wavelengths, whereas its derivatives feature two distinct adsorption maxima with a second one at a higher wavelength each. The splitting of the absorption maximum is caused by the halogen atoms introduced into the framework (Fig. 2 right). This second adsorption maximum shifts to higher wavelengths with increasing polarizability of the halogen atoms (from fluorine to iodine). Therefore, the novel UiO-66-$I_2$ exhibits the largest shift of this maximum. The successful incorporation of the linker molecules into the framework and the complete removal of solvents during work-up were verified with $^1$H-NMR-spectroscopy on digested samples (see ESI,‡ Fig. S4). In addition, the configuration of the 2,5-diiodo-1,4-dibenzoic acid linker molecule was verified with $^{13}$C-NMR-spectroscopy (see ESI,‡ Section 1 and Fig. S5). The recorded spectra substantiate that the phase-pure samples were solvent-free and that the linker molecules are not altered during solvothermal synthesis. Furthermore, the spectra of all derivatives show the incorporation of modulator molecules (formic acid) in the frameworks indicating missing linker defects.

Further analysis *via* argon physisorption measurements on the novel UiO-66-$I_2$ reveals the intact porosity of this framework after solvent exchange and activation (see ESI,‡ Fig. S1). A typical type I isotherm, characteristic for microporous materials like UiO-66 derivatives, was obtained, with a BET-surface area of roughly 500 m$^2$ g$^{-1}$ and a pore volume of 0.23 cm$^3$ g$^{-1}$. SEM images of UiO-66-$I_2$ show that the MOF crystallized in individual particles with a size below 100 nm (see ESI,‡ Fig. S2). From thermogravimetric analysis the thermal stability was found to be at a high temperature of 400 °C (see ESI,‡ Fig. S3).

### Structure of UiO-66 and its halogenated analogues

The DFT study presented is based on the generation of accurate structural models with precise representation of the experimental

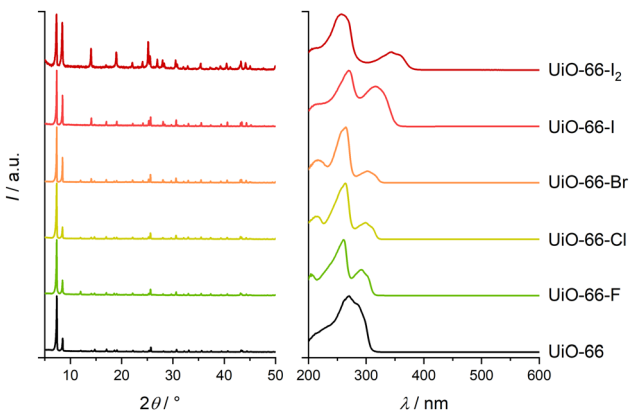


Fig. 2 PXRD patterns (left) and UV-Vis spectra (right) of UiO-66 and its mono- and dihalogenated derivatives.

Open Access Article. Published on 19 May 2023. Downloaded on 12/5/2025 2:59:33 AM.
This article is licensed under a Creative Commons Attribution 3.0 Unported Licence.

lattice parameters. The cubic phase of UiO-66 crystallizes in space group $F\bar{4}3m$ with an experimental lattice parameter of $a$ = 20.747 Å and contains four primitive triclinic cells ($a_P$ = 14.668 Å).[48] The monohalogenated UiO-66 derivatives and the novel diiodo derivative are isostructural with the parent UiO-66 and have closely matching lattice parameters as shown in the PXRD patterns (see Fig. 2). Hence, the lattice parameters of the fully relaxed cells of all derivatives were compared with the experimental ones of pristine UiO-66 to assess suitable XC functionals to obtain structural models (see ESI,‡ Section 3). In contrast to the unmodified UiO-66, all models of the halogenated derivatives have a reduced symmetry (space group $R3$), but share the primitive cell of UiO-66. The comparison of the lattice parameter $a_P$ of all UiO-66 type MOF models with the experimental value of UiO-66 resulted for all XC functionals in an error of less than 0.5%. The smallest error of 0.05% for the fully relaxed UiO-66 cell was observed with the rSCAN functional. In the case of all monohalogenated UiO-66 analogues, the use of the PBEsol-TS functional yielded models with an error of less than 0.1% in the lattice parameter $a_P$, while the PBEsol and rSCAN functional led to comparable results with errors larger than 0.3% (see ESI,‡ Table S1). The benchmark with the novel UiO-66-$I_2$ shows a different outcome, all functionals lead to structures with an error above 0.1%. The models generated with the PBEsol and PBEsol-TS functional indicate the steric demand of the two iodine atoms of the linker leading to a slight widening of the structure. The smallest error is achieved by choosing the rSCAN functional leading to a slight underestimation of the lattice parameter with an error of 0.13%. In total, a model with an error in the lattice parameter of approximately a tenth of a percent for all investigated UiO-66 type MOFs was generated (see ESI,‡ Table S1). This confirms the experimental PXRD study and underlines the robustness of the UiO-66 topology regarding the introduction of functional groups to the linker. Furthermore, the results of this benchmark show, that a decent basis set size is required to obtain a precise structural description of the MOFs and to predict the lattice parameters of novel MOFs.

### Electronic structure of UiO-66 and its halogenated analogues

It is well known, that the electronic structure of UiO-66 is altered by the use of functionalized linkers. The functionalization can be used to tune the band gap of the resulting materials and thus the optical properties of the UiO-66 derivatives.[25,31,49,50] This section deals with a detailed discussion of the electronic structures of the halogenated UiO-66 derivatives in order to understand the effects of the different halogenated linkers on the resulting MOFs.

On the basis of the fully relaxed structures, the electronic structures of UiO-66 and its halogenated derivatives were calculated employing the HSE06 hybrid DFT functional (see ESI,‡ Section 5). In a first step, we compared the calculated band gaps of UiO-66 with experimental values (see ESI,‡ Fig. S6 and Table S2) to validate the electronic structure calculations shown in Fig. 3. The band gap energies obtained from DFT calculations follow the trend of the measured ones and reproduce the experimental values in very good agreement. Furthermore, the theoretical band gap values of the monohalogenated

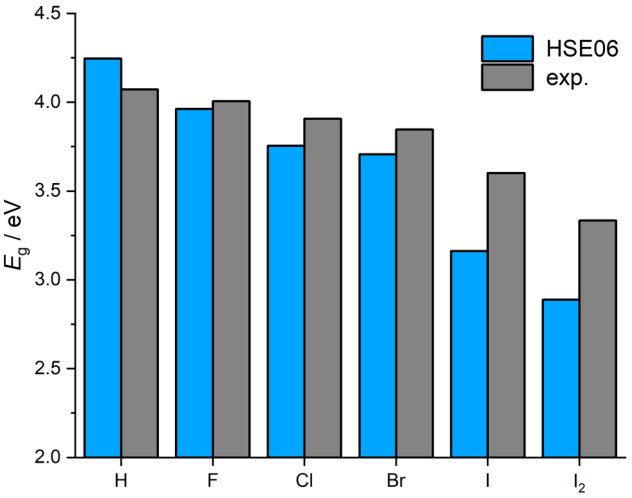


Fig. 3 Comparison of the calculated (HSE06) band gaps of UiO 66 and its halogenated derivatives with experimental (exp.) values.

UiO-66 analogues are consistent with the HSE06 values reported by Ni *et al.*[25] The comparison of the band gaps in Fig. 3 reveals that the experimental values of both iodo-based derivatives have an unexpected deviation of about 0.5 eV from the calculated values. A possible explanation for this discrepancy might be the fact, that the theoretical band gaps were calculated with ideal defect-free crystal structures, whereas the prepared samples might contain a larger numbers of missing linker defects due to the higher steric demand of the iodine-based linkers. The missing linker defects are compensated by the incorporation of modulator molecules into the framework, which is visible in the ESI,‡ Fig. S4 by the presence of formic acid. The effect of defects in UiO-66 on its electronic structure was already studied by Svane *et al.*[51] Moreover, the evaluation of band gaps of MOFs with UV-Vis DRS has some uncertainty, which can be seen in the values given for UiO-66-type MOFs in the literature.[31,50,52] Additionally, the switching of light sources in region between 300 and 375 nm introduces a possible error to the spectra of UiO-66-I and UiO-66-$I_2$ and the corresponding Tauc plots (see ESI,‡ Fig. S6). All in all, the trend of the calculated band gaps is in very good agreement with the experimental values.

The comparison of the band gaps in Fig. 3 shows clearly that the halogenation of the UiO-66 linker leads to a lowering of the band gap. This effect increases with the installation of heavier halogens and can be enhanced with the use of dihalogenated linkers. The following analysis of the calculated band structures, corresponding density of states (DOS) and projected density of states (PDOS) allows a deeper understanding.

In general, flat bands with almost no dispersion are typically observed for extended systems like MOFs. Starting with the band structure of UiO-66-F the effect of a halogenated linker is readily traceable. The density of states of the pristine UiO-66 shows a single maximum at the valence band maximum (VBM) which is mainly formed by the delocalized electrons of the aromatic system of the linker (see Fig. 4 and ESI,‡ Fig. S19). These VBM states are divided into two maxima in the case of the UiO-66-F. The VBM of the fluorinated UiO-66 is formed by

 This journal is © the Owner Societies 2023

Open Access Article. Published on 19 May 2023. Downloaded on 12/5/2025 2:59:33 AM.
This article is licensed under a Creative Commons Attribution 3.0 Unported Licence.

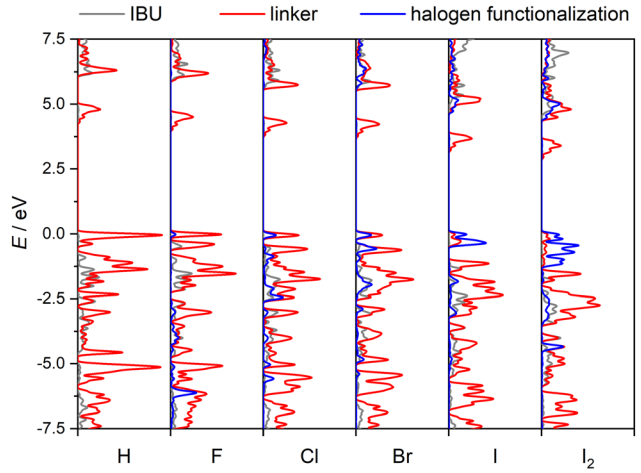


Fig. 4 PDOS of UiO-66, its monohalogenated derivatives and the novel compound UiO-66-$I_2$.

the free electrons of the fluorine atoms and delocalized electrons of the aromatic system depicted in Fig. 5. The second maximum at the VBM also consists of π-electrons of the aromatic system and free electrons of both, oxygen atoms at the carboxylate group of the linker as well as oxygen atoms incorporated into the IBU. The projected electron densities of both maxima are shown in Fig. 5(a) and (b). Simultaneously, the conduction band minimum (CBM) stays the same compared to the pristine UiO-66. These features are observed for every monohalogenated UiO-66 derivative. The p-electrons of the fluorine atoms are strongly bound leading only to a small number of associated states at the VBM. The effect by the fluorination of the linker is rather small on the parent UiO-66 band gap, which is only lowered by about 0.3 eV. For the same reason no significant changes in the polarizability of the UiO-66-F compared to the UiO-66 are expected, which in consequence will result in a comparable RI of the UiO-66-F compared to the pristine UiO-66.

The splitting of the VBM states observed for UiO-66-F increases for UiO-66-Cl (see Fig. 4 and ESI,‡ Fig. S21) and is caused by the weaker bound valence electrons of the chlorine atom. This leads to a further narrowing of the band gap. Additionally, the higher number of p-electrons of the chlorine atom leads to the formation of states at the second maximum at the VBM and more states at the low-energy region of the valence band (VB) resulting in a system with higher polarizability. The red shift of the band gap due to the larger splitting of the VBM states and the increased polarizability will finally lead to a higher RI in the visible region compared to the unmodified UiO-66 as shown below.

The introduction of bromine atoms leads only to a slightly smaller band gap compared to UiO-66-Cl ($\Delta E_g$ = 0.05 eV). Again, the CBM stays unchanged and compared to UiO-66-Cl the VBM states do not change notably as well. The splitting of states at the VBM does only increase slightly compared to the UiO-66-Cl, but the second maximum at the VBM is in turn more pronounced because of the weaker bound and larger number of p-electrons of the bromine atoms (see Fig. 4 and ESI,‡ Fig. S22). The higher number of states at the top of the VB results in an increased polarizability of the UiO-66-Br promoting also a higher RI in the visible region compared to the chloro analogue.

In contrast to the halogen derivatives already discussed, the VBM of the UiO-66-I shows more distinct features than two isolated maxima. The increased delocalization of the p-electrons of the iodine atoms results in a reduced energy of the corresponding states leading to a decomposition of the DOS maximum at the VBM into two maxima. These new VBM states are dominated by states of the iodine atoms (see Fig. 4 and 6). The analysis of the projected electron densities of these two DOS maxima at the VBM reveals that the splitting of the parent VBM states is caused by the two different orientations of the non-bonding p-orbitals of the iodine atom. The first maximum of those states at the VBM is mainly formed by the electrons of the p-orbitals of the iodine atom orientated perpendicular to the phenyl group of the *bdc* linker allowing a larger delocalization of the electrons *via* conjugation with the aromatic system (see Fig. 6a). The second maximum at the VBM of UiO-66-I is mainly formed by the electrons of the p-orbitals of the iodine atoms which are orientated parallel to the phenyl group of the *bdc* linker preventing a conjugation with the aromatic system and leading to more localized states with an higher energy (see Fig. 6b). Furthermore, the initial splitting of the VBM states into two isolated maxima observed at the monohalogenated UiO-66 analogues increases further leading to a notable reduction of the band gap compared to the UiO-66-Br of about 0.55 eV. In contrast to the other monohalogenated UiO-66 derivatives, the second maximum of the splitted VBM states of UiO-66-I is

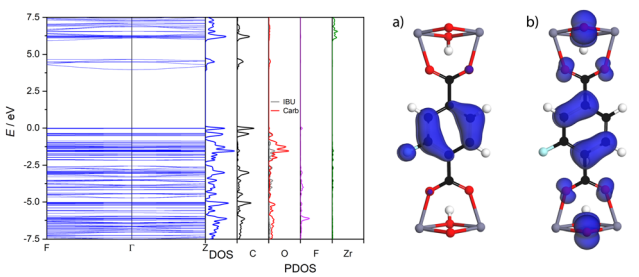


Fig. 5 Band structure, DOS and PDOS of UiO-66-F and projected electron densities of (a) the first and (b) the second DOS maximum of the VBM (isosurface value 0.04 e Å$^{-3}$).

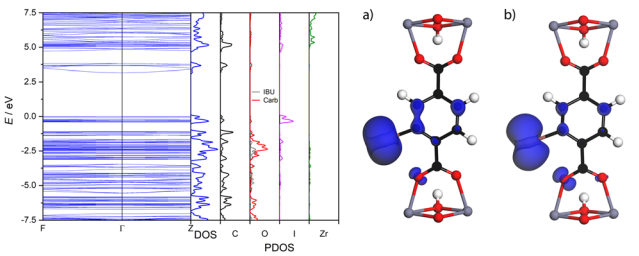


Fig. 6 Band structure, DOS and PDOS of UiO-66-I and projected electron densities of (a) the first and (b) the second DOS maximum at the VBM (isosurface value 0.04 e Å$^{-3}$).

Open Access Article. Published on 19 May 2023. Downloaded on 12/5/2025 2:59:33 AM.
This article is licensed under a Creative Commons Attribution 3.0 Unported Licence.

located at about −1 eV. This maximum is formed mainly by states of the aromatic system. The delocalized states of the halogen atoms are now located at the VBM because of the diffuse character of the p-electrons of the iodine atom. The large number of delocalized states at the VBM leads to a system with high polarizability. Additionally, the band gap is diminished further resulting in a material with a high RI.

The introduction of a second iodine atom to the iodo *bdc* linker leads to the novel MOF UiO-66-$I_2$ whose band gap is about 0.3 eV smaller compared to the UiO-66-I. In contrast to the discussed electronic structures of the monohalogenated UiO-66 analogues no splitting of the states at the VBM can be observed (see Fig. 4 and ESI,‡ Fig. S24). In case of the diiodo UiO-66 derivative, the introduction of the large number of delocalized p-electrons by the iodine atoms leads to a domination of those at the top of the VB, the splitting of states at the VBM vanish. The electrons of the aromatic system of the *bdc* linker are still located at about −1 eV. A detailed analysis of the iodine atom states at the top of the VB reveals the occurrence of a fine splitting. Here, the first two maxima of the UiO-66-I VBM are still present, but each of those parent maxima shows two new maxima. Comparable to UiO-66-I the first group of two maxima at the VBM originates from p-orbitals of the iodine atoms that are perpendicular to the benzene ring of the linker and are delocalized due to conjugation. The second set of maxima belongs to p-orbitals of the iodine atoms that are parallel orientated to the aromatic system of the linker. The observed fine splitting at the VBM states of UiO-66-$I_2$ is caused by different linker orientations. The first maximum of each pair of maxima belongs to linker that show no rotation and are parallel orientated to the plane of the corresponding carboxylate groups. The second maximum of those pairs belongs to linker molecules that are rotated out of the plane of the corresponding carboxylate groups. This different linker orientations are observed due to the steric demand of the two iodine atoms per linker preventing a simultaneous in-plane orientation of all linker molecules. Furthermore, the underlying UiO-66-$I_2$ model possess two groups of symmetry equivalent linkers leading to the observation of only two distinct linker orientations. Thus, the fine splitting of the VBM states is only an artifact and has no relevant influence on the electronic structure and the resulting optical properties. The fine splitting of VBM states will vanish for a dynamic model without symmetry constraints featuring a broad range of different linker orientations. Finally, the large amount of states introduced to the VBM combined with the further reduced band gap result in a highly polarizable system and thus the resulting UiO-66-$I_2$ shows further tuned optical properties. This underlines the tuneability of the optical properties of the monohalogenated UiO-66 frameworks by the introduction of a second halogen atom to the linker.

### Optical properties of UiO-66 and its halogenated analogues

Applying the HSE06 hybrid DFT functional we calculated the dielectric function and subsequently the complex refractive index of UiO-66 and its mono- and dihalogenated derivatives. The dispersion curves of the refractive indices (RI) in the visible range and the values at the sodium D-line (589 nm) of the investigated UiO-66 analogues are shown in Fig. 7. The impressively wide range of RI values covered with the halogenated UiO-66 derivatives shows clearly the potential of MOFs as optical materials and highlights the linker functionalization as versatile method to tune the optical properties of MOFs within a given framework topology.

The RI of UiO-66 and its monohalogenated derivatives show the typical normal dispersion of optical materials in the visible range due to the absorption of UV light. The RI dispersion of UiO-66 and UiO-66-F are almost identical in the visible region (1.37 and 1.38 at 589 nm) but differ towards the UV region. On the one hand this is caused by the comparable polarizabilities of the *bdc* and *bdc*-F linkers resulting in similar values for the static refractive index. On the other hand, the UiO-66-F has a reduced band gap compared with UiO-66 leading to a red shift of the absorption maximum and thus of a red shift of the maximum of the RI. This shift leads to differences of the RI of UiO-66 and UiO-66-F in the blue light and UV region, in which

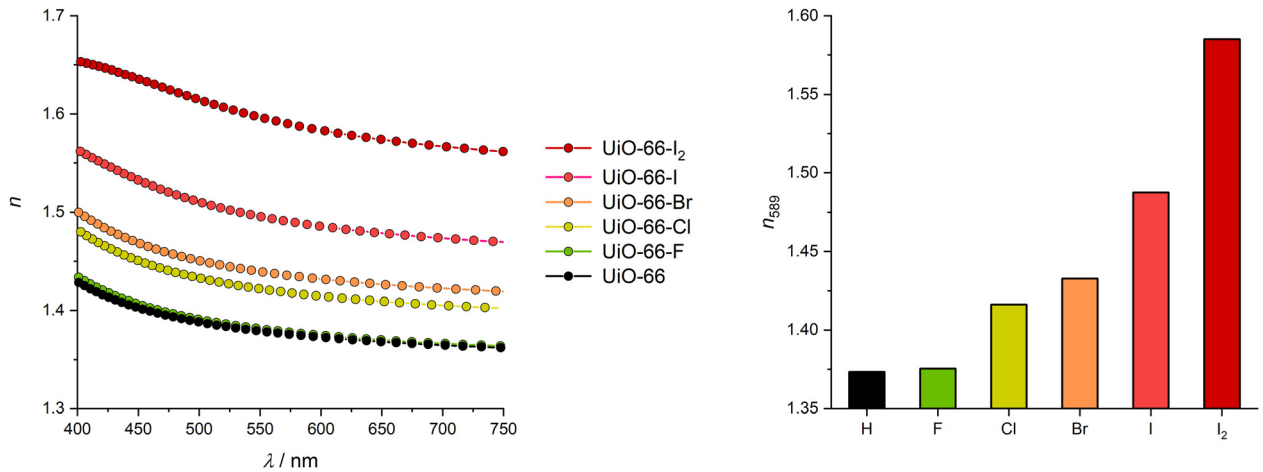


Fig. 7 Calculated refractive index of UiO-66 and its mono- and dihalogenated derivatives: dispersion curves of the refractive index (left) and values at the sodium D-line (589 nm) (right).

 This journal is © the Owner Societies 2023

Open Access Article. Published on 19 May 2023. Downloaded on 12/5/2025 2:59:33 AM.
This article is licensed under a Creative Commons Attribution 3.0 Unported Licence.

the UiO-66-F has higher RI values. The similarity of the RI values of UiO-66 and its flouro analogue were also reported by Ni *et al.* with values of 1.476 and 1.484, respectively.[25] The discrepancy in absolute values is caused by the calculation method by Ni *et al.*, who used a combination of the PBE GGA functional and a scissors operator to correct the underestimation of the band gap by the PBE functional. This approach might be suitable to determine trends in the RI, but lacks a precise description of the optical properties. To obtain a precise description of the optical properties further corrections are required to satisfy the sum rule, since the sole use of the scissors operator leads to overestimated amplitudes in the dielectric function resulting in higher values of the RI.[36]

In contrast to the UiO-66-F, the introduction of a chlorine or bromine atom leads to a remarkable increase of the RI (see Fig. 7). Both materials, UiO-66-Cl as well as UiO-66-Br show reduced band gaps compared to the UiO-66-F and higher electron densities at the VBM. This results in systems with a red shifted maximum of the RI and higher polarizability promoting higher RI values in the visible region of the light. The RI of the chloro and bromo derivatives are 1.42 and 1.43 at 589 nm, respectively, corresponding to an increase of the RI compared to the parent UiO-66 of about 0.04 due to the chloro functionalization. Substitution of the chlorine atoms with bromine atoms leads to a further increase of about 0.02 in the RI. These raises of the RI are consistent with the values of Ni *et al.*, whereas the absolute values differ as pointed out before.[25] The increase of the RI due to the incorporation of chlorine atoms instead of fluorine atoms is twice times higher than the effect of the substitution of the chlorine atoms with bromine atoms. This can be ascribed to two factors. First the introduction of chlorine instead of fluorine atoms is followed by a large increase of the electron density at the VBM while the substitution of chlorine with bromine atoms has less effect on the VBM states, since the new states are not located directly at the VBM. Second, the redshift of the band gap energy by the chlorine substitution is four times larger compared to the red shift caused by the bromo substitution, resulting in similar RI values for UiO-66-Cl and UiO-66-Br.

The substitution of the bromine with iodine atoms allows a further tuning of the RI. UiO-66-I shows a RI of 1.49 at 589 nm corresponding to an increase of about 0.05 compared to UiO-66-Br being in line with the reported increment of Ni *et al.*[25] This relatively large increase in the RI is caused by the large polarizability of the iodo functionalized linker which is a result of the large number of delocalized iodine states at the VBM coupled with an additional decrease of the band gap. The band gap of the UiO-66-I is close to the visible range of the light, shifting the maximum of the RI analogously towards to the visible range causing high RI values.

The introduction of a second iodine atom to the *bdc*-I linker results in the UiO-66-$I_2$ MOF featuring a linker with a large polarizability. This leads to an even larger RI value of 1.59 at 589 nm which is an increase of the RI of UiO-66-I of 0.1 and opens up the field for advanced optical systems requiring a large modulation of the RI. The application of the UiO-66-$I_2$ is only limited by its absorption of blue light visible as a plateau in the dispersion of the RI. This absorption at the edge of the visible range is caused by the band gap reduction due to the introduction of a second iodine atom to the linker, although this red shift of the band gap next to the large density of states at the VBM enables the large RI values of this material.

Overall, the functionalization of UiO-66 by halogenation of the *bdc* linker leads to promising derivatives for optical applications sharing the high chemical stability of the parent material. While UiO-66-F shows only differences of the RI in the UV region, all other mono- and dihalogenated UiO-66 analogues described above allow a broad range tuning of the RI in the visible light within a single crystal topology. Furthermore, the halogenation of the *bdc* linker not only leads to UiO-66 type MOFs with a broad range of RI, but additionally preserves the porosity of the framework resulting in versatile materials for optical applications. This allows the use of these materials for example in the construction of optical filters of coating as well as optical gas sensors due to their porosity *e.g.* by the coating of waveguides. Finally, this study makes reliable RI values for UiO-66 and its derivatives available. In 2018, Hunag *et al.* published a first attempt to characterize the RI of UiO-66, but the used films were not of optical quality and the complete removal of solvents out of the porosity was not monitored.[53] Here, with the presented optical properties in this study the development and calculation of optical systems incorporating UiO-66 materials is facilitated.

## Conclusions

The functionalization of the Zr-based UiO-66 MOF *via* halogenation of the *bdc* linker was studied. The resulting monohalogenated derivatives as well as a novel diiodo derivative were characterized *via* their electronic structures and the resulting optical properties. For this purpose, we applied our previously established simulation approach featuring the HSE06 hybrid DFT functional. Furthermore, we report the successful synthesis and characterization of the novel UiO-66-$I_2$ MOF which contains a *bdc* linker with two iodine atoms in *para* position.

Deploying accurate converged plane-wave basis sets with respect to the total energy and the lattice parameters of the systems, fully relaxed periodic models were generated by assessing different XC functionals to obtain precise representations of the investigated materials. All halogenated derivatives are found to be isostructural and have comparable lattice parameters underlining the versatile and modular design of MOFs. Subsequently, electronic structure calculations were performed and the obtained band gap energies were validated with UV-Vis DRS measurements. The closely matching experimental and theoretical band gaps ensure a reliable calculation of the refractive index in the next step. The use of halogenated linkers leads to a series of decreasing band gaps with increasing size of the halogen atom which can be enhanced by introducing two halogen atoms to a single linker. To gain a deeper understanding of the electronic structure, the materials were

Open Access Article. Published on 19 May 2023. Downloaded on 12/5/2025 2:59:33 AM.
This article is licensed under a Creative Commons Attribution 3.0 Unported Licence.

analyzed *via* PDOS revealing that the halogenation of the *bdc* linker leads to a splitting of the VBM states. The electron density in this region increases with the introduction of heavier halogen atoms leading to higher polarizabilities. Afterwards the dispersion curves of the RI were calculated at hybrid DFT level. The differences in the RI of the different derivatives were characterized and reduced to the reduction of the band gap energies and introduction of more delocalized states at the VBM due to the incorporation of more diffuse halogen atoms.

Overall, this work underlines the potential of MOFs as optical materials offering a broad range of accessible refractive indices. The halogenation of linkers was proven to be a simple but effective method to exploit the modular design of MOFs to obtain materials with tailored optical properties. This allows the use of MOFs in several optical systems like filters requiring high and low refracting materials in a single design. Especially in systems with layered designs MOFs have great potential offering different RI values within a single topology and synthesis protocol. Furthermore, the halogenation of the linkers preserves the porosity of the framework enabling the incorporation of guest molecules to further tune the RI or perform sensing. Additionally, the halogenated derivatives are transparent in the visible range of the light and some of them even enable applications in the UV region widening up the field of possible applications.

## Conflicts of interest

There are no conflicts to declare.

## Acknowledgements

We acknowledge the support of the cluster system team at the Leibniz University of Hannover, Germany in the production of this work. This work is funded by the DFG under Germany's Excellence Strategy within the Cluster of Excellence PhoenixD (EXC 2122, Project ID 390833453). A. H. is grateful for being funded by the Hannover School for Nanotechnology (HSN) at the Laboratory of Nano and Quantum Engineering (LNQE). The HSN is funded by the Ministry of Science and Culture of Lower Saxony.

## Notes and references

1 J. L. Rowsell and O. M. Yaghi, *Microporous Mesoporous Mater.*, 2004, **73**, 3.
2 S. R. Batten, N. R. Champness, X.-M. Chen, J. Garcia-Martinez, S. Kitagawa, L. Öhrström, M. O'Keeffe, M. Paik Suh and J. Reedijk, *Pure Appl. Chem.*, 2013, **85**, 710.
3 L. E. Kreno, K. Leong, O. K. Farha, M. Allendorf, R. P. van Duyne and J. T. Hupp, *Chem. Rev.*, 2012, **112**, 1105.
4 H. Li, K. Wang, Y. Sun, C. T. Lollar, J. Li and H.-C. Zhou, *Mater. Today*, 2018, **21**, 108.
5 A. Dhakshinamoorthy, Z. Li and H. Garcia, *Chem. Soc. Rev.*, 2018, **47**, 8134.
6 T. N. Nguyen, F. M. Ebrahim and K. C. Stylianou, *Coord. Chem. Rev.*, 2018, **377**, 259.
7 Y. Zheng, F.-Z. Sun, X. Han, J. Xu and X.-H. Bu, *Adv. Opt. Mater.*, 2020, **8**, 2000110.
8 K.-T. Hsu, P. Thanasekaran, T.-W. Hsu, C.-H. Su, B.-C. Chang, Y.-H. Liu, C.-H. Hung and K.-L. Lu, *CrystEngComm*, 2021, **23**, 824.
9 H. Li, L. Zhang, H. He, Y. Yang, Y. Cui and G. Qian, *Sci. China: Mater.*, 2021, **64**, 698.
10 K. Hendrickx, D. E. P. Vanpoucke, K. Leus, K. Lejaeghere, A. van Yperen-De Deyne, V. van Speybroeck, P. van der Voort and K. Hemelsoet, *Inorg. Chem.*, 2015, **54**, 10701.
11 M. A. Syzgantseva, C. P. Ireland, F. M. Ebrahim, B. Smit and O. A. Syzgantseva, *J. Am. Chem. Soc.*, 2019, **141**, 6271.
12 W. Yin, C.-A. Tao, F. Wang, J. Huang, T. Qu and J. Wang, *Sci. China: Mater.*, 2018, **61**, 391.
13 M. D. Allendorf, M. E. Foster, F. Léonard, V. Stavila, P. L. Feng, F. P. Doty, K. Leong, E. Y. Ma, S. R. Johnston and A. A. Talin, *J. Phys. Chem. Lett.*, 2015, **6**, 1182.
14 E. Redel, Z. Wang, S. Walheim, J. Liu, H. Gliemann and C. Wöll, *Appl. Phys. Lett.*, 2013, **103**, 91903.
15 N. C. Keppler, K. D. J. Hindricks and P. Behrens, *RSC Adv.*, 2022, **12**, 5807.
16 J. E. Ellis, S. E. Crawford and K.-J. Kim, *Mater. Adv.*, 2021, **2**, 6169.
17 Y. Bai, Y. Dou, L.-H. Xie, W. Rutledge, J.-R. Li and H.-C. Zhou, *Chem. Soc. Rev.*, 2016, **45**, 2327.
18 J. H. Cavka, S. Jakobsen, U. Olsbye, N. Guillou, C. Lamberti, S. Bordiga and K. P. Lillerud, *J. Am. Chem. Soc.*, 2008, **130**, 13850.
19 F. Vermoortele, M. Vandichel, B. van de Voorde, R. Ameloot, M. Waroquier, V. van Speybroeck and D. E. de Vos, *Angew. Chem., Int. Ed.*, 2012, **51**, 4887.
20 M. Kandiah, M. H. Nilsen, S. Usseglio, S. Jakobsen, U. Olsbye, M. Tilset, C. Larabi, E. A. Quadrelli, F. Bonino and K. P. Lillerud, *Chem. Mater.*, 2010, **22**, 6632.
21 S. J. Garibay and S. M. Cohen, *Chem. Commun.*, 2010, **46**, 7700.
22 S. Biswas, J. Zhang, Z. Li, Y.-Y. Liu, M. Grzywa, L. Sun, D. Volkmer and P. van der Voort, *Dalton Trans.*, 2013, **42**, 4730.
23 W. Liang, R. Babarao and D. M. D'Alessandro, *Inorg. Chem.*, 2013, **52**, 12878.
24 L. Shen, R. Liang, M. Luo, F. Jing and L. Wu, *Phys. Chem. Chem. Phys.*, 2015, **17**, 117.
25 B. Ni, W. Sun, J. Kang and Y. Zhang, *J. Phys. Chem. C*, 2020, **124**, 11595.
26 C. Zhu, R. E. Gerald and J. Huang, *IEEE Sens. J.*, 2021, **21**, 19647.
27 H.-Y. Pan, X. Chen and X.-L. Xia, *Renewable Sustainable Energy Rev.*, 2022, **161**, 112361.
28 A. K. Oskouei, L. A. Emmert, W. Rudolph, M. Steinecke, M. Jupé, L. O. Jensen and D. Ristau, *Optical Interference Coatings Conference (OIC)*, OSA, Washington, DC, ThB.2, 2019.
29 H. K. Raut, V. A. Ganesh, A. S. Nair and S. Ramakrishna, *Energy Environ. Sci.*, 2011, **4**, 3779.

Open Access Article. Published on 19 May 2023. Downloaded on 12/5/2025 2:59:33 AM.
This article is licensed under a Creative Commons Attribution 3.0 Unported Licence.

30 Y. Kokubun, N. Funato and M. Takizawa, *IEEE Photon. Technol. Lett.*, 1993, **5**, 1297.
31 M. Treger, A. Hannebauer, A. Schaate, J. L. Budde, P. Behrens and A. M. Schneider, *Phys. Chem. Chem. Phys.*, 2023, **25**, 6333.
32 S. Biswas and P. van der Voort, *Eur. J. Inorg. Chem.*, 2013, 2154.
33 A. V. Krukau, O. A. Vydrov, A. F. Izmaylov and G. E. Scuseria, *J. Chem. Phys.*, 2006, **125**, 224106.
34 J. Paier, M. Marsman, K. Hummer, G. Kresse, I. C. Gerber and J. G. Ángyán, *J. Chem. Phys.*, 2006, **125**, 249901.
35 A. J. Garza and G. E. Scuseria, *J. Phys. Chem. Lett.*, 2016, **7**, 4165.
36 M. Nishiwaki and H. Fujiwara, *Comput. Mater. Sci.*, 2020, **172**, 109315.
37 K. Cui, J. Ma, X.-K. Huo and J.-X. Zhang, *Z. Naturforsch. B*, 2014, **69**, 859.
38 G. C. Shearer, S. Chavan, J. Ethiraj, J. G. Vitillo, S. Svelle, U. Olsbye, C. Lamberti, S. Bordiga and K. P. Lillerud, *Chem. Mater.*, 2014, **26**, 4068.
39 J. Chu, F.-S. Ke, Y. Wang, X. Feng, W. Chen, X. Ai, H. Yang and Y. Cao, *Commun. Chem.*, 2020, **3**, 5.
40 W. Kohn and L. J. Sham, *Phys. Rev.*, 1965, **140**, A1133–A1138.
41 S. J. Clark, M. D. Segall, C. J. Pickard, P. J. Hasnip, M. I. J. Probert, K. Refson and M. C. Payne, *Z. Kristallogr.*, 2005, **220**, 567.
42 D. D. Koelling and B. N. Harmon, *J. Phys. C: Solid State Phys.*, 1977, **10**, 3107.
43 J. P. Perdew, A. Ruzsinszky, G. I. Csonka, O. A. Vydrov, G. E. Scuseria, L. A. Constantin, X. Zhou and K. Burke, *Phys. Rev. Lett.*, 2008, **100**, 136406.
44 W. A. Al-Saidi, V. K. Voora and K. D. Jordan, *J. Chem. Theory Comput.*, 2012, **8**, 1503.
45 A. P. Bartók and J. R. Yates, *J. Chem. Phys.*, 2019, **150**, 161101.
46 A. J. Morris, R. J. Nicholls, C. J. Pickard and J. R. Yates, *Comput. Phys. Commun.*, 2014, **185**, 1477.
47 A. Schaate, P. Roy, A. Godt, J. Lippke, F. Waltz, M. Wiebcke and P. Behrens, *Chem. – Eur. J.*, 2011, **17**, 6643.
48 S. Øien, D. Wragg, H. Reinsch, S. Svelle, S. Bordiga, C. Lamberti and K. P. Lillerud, *Cryst. Growth Des.*, 2014, **14**, 5370.
49 K. Hendrickx, D. E. P. Vanpoucke, K. Leus, K. Lejaeghere, A. van Yperen-De Deyne, V. van Speybroeck, P. van der Voort and K. Hemelsoet, *Inorg. Chem.*, 2015, **54**, 10701.
50 E. Flage–Larsen, A. Røyset, J. H. Cavka and K. Thorshaug, *J. Phys. Chem. C*, 2013, **117**, 20610.
51 K. L. Svane, J. K. Bristow, J. D. Gale and A. Walsh, *J. Mater. Chem. A*, 2018, **6**, 8507.
52 T. Musho, J. Li and N. Wu, *Phys. Chem. Chem. Phys.*, 2014, **16**, 23646.
53 Y. Huang, C.-A. Tao, R. Chen, L. Sheng and J. Wang, *Nanomaterials*, 2018, **8**, 676.